

# QCD Predictions for Event-Shape Distributions in Hadronic Higgs Decays

---

**G. Coloretti,<sup>a</sup> A. Gehrmann–De Ridder,<sup>a,b</sup> C. T. Preuss<sup>a</sup>**

<sup>a</sup>*Institute for Theoretical Physics, ETH, CH-8093 Zürich, Switzerland*

<sup>b</sup>*Department of Physics, University of Zürich, CH-8057 Zürich, Switzerland*

*E-mail:* [guglielmo.coloretti@math.ethz.ch](mailto:guglielmo.coloretti@math.ethz.ch), [gehra@phys.ethz.ch](mailto:gehra@phys.ethz.ch),  
[cpreuss@phys.ethz.ch](mailto:cpreuss@phys.ethz.ch)

**ABSTRACT:** We study the six classical event-shape observables in hadronic Higgs decays at next-to-leading order in QCD. To this end, we consider the decay of on-shell Higgs bosons to three partons, taking into account both the Yukawa-induced decay to b-quark pairs and the loop-induced decay to two gluons via an effective Higgs-gluon coupling. The results are discussed with a particular focus on the discriminative power of event shapes regarding these two classes of processes.

---

## Contents

<b>1</b>	<b>Introduction</b>	<b>1</b>
<b>2</b>	<b>Differential Higgs decay rates at NLO in QCD</b>	<b>4</b>
2.1	General framework	6
2.2	Yukawa-type contributions	7
2.3	Effective-theory-type contributions	8
2.4	Validation	8
<b>3</b>	<b>Numerical Results</b>	<b>9</b>
3.1	Numerical set-up and scale-variation prescription	10
3.2	Differential predictions for Higgs-decay event-shape observables	11
3.3	Comparison to $(Z/\gamma)^*$ decays	18
<b>4</b>	<b>Summary and Outlook</b>	<b>20</b>

---

## 1 Introduction

The Higgs boson was discovered by the ATLAS and CMS experiments at CERN in 2012 [1, 2]. Since then, a major goal of present and future collider-physics programmes is the precise determination of Higgs-boson properties and the in-depth validation of the Higgs mechanism of electroweak symmetry breaking. For the latter, one needs to firmly establish that the masses of all fundamental particles are generated through their interaction with the Higgs boson through precision measurements of each particle’s coupling strength. Up to now, the coupling of the Higgs boson to the electroweak gauge bosons  $Z$  and  $W^\pm$ , as well as to third-generation fermions (bottom and top quarks, tau leptons) have been established at the LHC, and the associated coupling strengths were measured. Within uncertainties, the properties and couplings of the Higgs boson are consistent with the predictions of the Standard Model of particle physics. Detailed and comprehensive reports on the status of analyses of current and expected LHC data pertaining to the Higgs boson can be found in [3, 4].

While the upcoming high-luminosity phase of the LHC (HL-LHC) will improve upon many of these measurements, some properties will remain elusive. Several Higgs-coupling measurements will be limited to accuracies around ten percent or above by the complexity related to the associated final states in hadronic collisions and their background processes. This accuracy is neither sufficient for real precision tests of the Higgs mechanism nor for testing scenarios for physics beyond the Standard Model, where one often expects deviations in the Higgs couplings at the level of at most few percents.

In-depth precision studies of the Higgs boson and the associated Higgs mechanism will become possible at a future electron-positron collider that operates at a collision energy at or above 240 GeV, see [5, 6] for details. The currently investigated CERN FCC-ee [5], CEPC [7], and ILC [8] projects are all aiming to operate as Higgs factories, *i.e.*, to produce a very large number of Higgs bosons for precision studies of its properties and couplings.

The striking advantage of  $e^+e^-$  colliders comes from their clean experimental environment, where interactions take place at well-defined centre-of-mass energies and background processes are significantly suppressed compared to hadron-collider environments.

A future  $e^+e^-$  collider will in particular enable model-independent measurements of the Higgs coupling to gauge bosons and fermions at the level of a few percent. It is expected that it will become possible to measure all decay channels of the Higgs boson, allowing for the precise determination of the total Higgs width. This is in stark contrast to the current situation at hadron colliders where only specific decay channels can be identified and reconstructed reliably.

The  $H \rightarrow b\bar{b}$  decay was observed at the LHC by the ATLAS [9] and CMS [10] collaborations in the  $VH$  ( $V = Z, W^\pm$ ) production modes with a significance of 5.3 and 5.6 standard deviations, respectively. This decay is extremely important to measure, as it not only provides a direct measurement of the Higgs coupling to fermions, but also constitutes the dominant contribution to the total Higgs width. While it is difficult to measure hadronic Higgs decays in inclusive Higgs production via the leading gluon-fusion and vector-boson-fusion production modes at the LHC, the measurement of the  $H \rightarrow b\bar{b}$  decay was facilitated by the presence of a leptonically decaying vector boson in the  $VH$  processes, which provides a clean experimental signature. A similar approach to measure the sub-dominant  $H \rightarrow gg$  decay at the LHC is, on the other hand, hindered by the overwhelming QCD background, despite impressive progress in distinguishing jets stemming from the Higgs decay from those originating from QCD background, see for example [11–15].

Hadronic Higgs decays mainly proceed via two decay modes: either as a Yukawa-induced decay to a bottom-quark pair or as a loop-induced decay to two gluons. Inclusive

hadronic decay widths of the Higgs are theoretically known up to fourth order in the strong coupling [16–23] in the (massless) b-quark channel and up to third order in the di-gluon channel [24–27] under the assumption of an infinitely heavy top quark, with first-order electroweak corrections known in both cases [28–35]. Fully-differential second-order calculations, with massless b-quarks, have been performed for both the production and the decay of the Higgs into a bottom-quark pair [36–38], as well as the combination with resummation [39] or parton showers [40]. In addition, the fully-differential  $H \rightarrow b\bar{b}$  decay rate has recently been computed at third order in the strong coupling [41], however without flavour identification, on which the other fixed-order calculations heavily relied.

We here wish to focus on global event-shape distributions related to hadronic Higgs decays, which can be regarded as a class of “good observables”. On the experimental side, event shapes can be reconstructed from hadron momenta without the need to use a jet algorithm. Those can directly access the geometrical event properties, with different event-shapes variables probing different aspects of the underlying parton-level dynamics. On the theory side, event shapes can be calculated reliably order-by-order in perturbative QCD and predictions can be compared faithfully with data away from the two-jet limit where resummation effects need to be taken into account. At LEP, global event-shape distributions were studied extensively in  $Z/\gamma$  decays as a vital tool for QCD precision measurements, as for instance for the determination of the strong coupling [42, 43] using the perturbative computations from [44, 45].

To the best of our knowledge, comparable precision calculations of event-shape observables for hadronic Higgs decays have not been made public so far. It is the purpose of this work to provide a comprehensive study of event-shapes in hadronic Higgs decays by computing the six classical event shapes: thrust,  $C$ -parameter, total and wide jet broadening, heavy-jet mass, and Durham three-jet resolution, at next-to-leading order (NLO) in QCD.

As a practical application of our work, we wish to study the suitability of event-shape observables as discriminators between both hadronic Higgs-decay modes, as a means to facilitate the extraction of the involved Higgs couplings. A similar idea has so-far only been pursued for the thrust observable, using either a three-jet merged calculation in [46] or an NLO calculation with approximate next-to-next-to-leading order (NNLO) effects in [47], and for the energy-energy correlation, which has been computed at NLO in [48, 49].

The structure of the paper is as follows: in section 2, we summarise the general framework of the calculation and provide details on all ingredients entering the computation of differential Higgs decays in perturbative QCD. Our results are presented in section 3

and summarised in section 4, where an outlook on future work is given as well.

## 2 Differential Higgs decay rates at NLO in QCD

In this work, we compute differential Higgs decay rates in the limit of vanishing light-quark masses, while keeping a non-vanishing Yukawa coupling only for the bottom quark and an infinitely large top-quark mass. As a consequence, the hadronic decay of the Higgs boson can be classified at parton level into two categories.

In the first category, the Higgs decay is associated to the Yukawa-type coupling  $y_b$ , and the decay can be obtained using the Standard-Model QCD Lagrangian. Being generated by a primary  $Hb\bar{b}$  vertex, contributions of this type will be referred to as belonging to the  $H \rightarrow b\bar{b}$  category in the remainder of this paper. The associated two-parton decay diagram is shown in the left-hand panel of fig. 1. Further, the corresponding three- and four-parton processes entering our calculation at LO and NLO are presented in the first column of table 1, while representative Feynman diagrams at tree and one-loop level are displayed in fig. 2.

The coupling to quarks also enables the Higgs boson to couple to gluons via a heavy-quark loop. In the limit of infinitely heavy top quarks, these top-quark loops decouple, yielding an effective theory containing a direct interaction of the Higgs field with the gluon field-strength tensor. In this second category, the interaction is mediated by an effective Hgg vertex, represented as a crossed dot in the right-hand panel of fig. 1. We shall refer to this type of contributions as belonging to the  $H \rightarrow gg$  category. It is worth mentioning that in this category there are two distinct tree-level processes contributing to the three-parton rate. A three-parton state can either be obtained via the emission of an additional gluon from the Hgg effective vertex or through the splitting of one of the primary gluons to a quark-antiquark pair. A summary of the three- and four-parton processes contributing to this decay category, entering our computation at LO and NLO, are presented in the second column of table 1, while corresponding representative diagrams at tree- and loop-level are displayed in fig. 3.

The above discussion can be implemented using an effective Lagrangian including both decay categories:

$$\mathcal{L}_{\text{Higgs}} = -\frac{\lambda(M_t, \mu_R)}{4} H G_{\mu\nu}^a G^{a,\mu\nu} + \frac{y_b(\mu_R)}{\sqrt{2}} H \bar{\psi}_b \psi_b. \quad (2.1)$$

Here, the effective Higgs-gluon coupling proportional to  $\alpha_s$  is written in terms of the Higgs vacuum expectation value  $v$  as,

$$\lambda(M_t, \mu_R) = -\frac{\alpha_s(\mu_R) C(M_t, \mu_R)}{3\pi v} \quad (2.2)$$

and the  $Hb\bar{b}$  Yukawa coupling is given as

$$y_b(\mu_R) = \bar{m}_b(\mu_R) \frac{4\pi\alpha}{\sqrt{2}M_W \sin\theta_W}. \quad (2.3)$$

As indicated by the  $\mu_R$  arguments, these quantities are subject to renormalisation. Throughout, we work in the  $\overline{\text{MS}}$  scheme and evaluate renormalised quantities at the renormalisation scale  $\mu_R$  with  $N_F = 5$ . While the top-quark Wilson coefficient  $C(M_t, \mu_R)$  is known up to order  $\alpha_s^4$  [25, 26, 50–54], it suffices to consider the first-order expansion for our purposes, *i.e.*,

$$C(M_t, \mu_R) = 1 + C^{(1)}(M_t, \mu_R) \frac{\alpha_s(\mu_R)}{2\pi} + \mathcal{O}(\alpha_s^2) = 1 + \frac{11}{6}N_C \frac{\alpha_s(\mu_R)}{2\pi} + \mathcal{O}(\alpha_s^2), \quad (2.4)$$

which is independent of the top-quark mass  $M_t$ . The running of the Yukawa mass  $\bar{m}_b$  is taken into account using the results of [55].

Before further discussing the details of our calculation for each decay category, we wish to highlight that the two terms present in eq. (2.1) do not interfere in the approximation of kinematically massless quarks, as considered here. When computing squared amplitudes, the operators present in eq. (2.1) neither interfere nor mix with each other under renormalisation [47]. In particular, this allows us to calculate higher-order QCD corrections for both decay channels independently and it renders the separate treatment of parton-level processes well-defined at each order.

We further wish to mention that in order to compare results in the  $H \rightarrow b\bar{b}$  and  $H \rightarrow gg$  decay modes, we will rescale the differential decay rates computed in both categories by their respective branching ratios, defined as

$$\text{Br}_{H \rightarrow b\bar{b}}^n(s, \mu_R) = \frac{\Gamma_{H \rightarrow b\bar{b}}^n(s, \mu_R)}{\Gamma_{H \rightarrow b\bar{b}}^n(s, \mu_R) + \Gamma_{H \rightarrow gg}^n(s, \mu_R)}, \quad (2.5)$$

$$\text{Br}_{H \rightarrow gg}^n(s, \mu_R) = \frac{\Gamma_{H \rightarrow gg}^n(s, \mu_R)}{\Gamma_{H \rightarrow b\bar{b}}^n(s, \mu_R) + \Gamma_{H \rightarrow gg}^n(s, \mu_R)}, \quad (2.6)$$

with  $n = 0, 1$  to be considered at LO and NLO, respectively. At LO, the inclusive hadronic  $H \rightarrow 2j$  decay widths read

$$\Gamma_{H \rightarrow b\bar{b}}^0(\mu_R) = \frac{y_b^2(\mu_R)M_H N_C}{8\pi}, \quad \Gamma_{H \rightarrow gg}^0(\mu_R) = \frac{\alpha_s^2(\mu_R)G_F M_H^3}{36\pi^3\sqrt{2}}, \quad (2.7)$$

where  $G_F$  is the Fermi constant and  $M_H$  the Higgs mass. Their first-order QCD corrections are known since long, *cf. e.g.* [16–27], and are given by

$$\Gamma_{H \rightarrow b\bar{b}}^1(s, \mu_R) = \Gamma_{H \rightarrow b\bar{b}}^0(\mu_R) \left[ 1 + \left( \frac{\alpha_s(\mu_R)}{2\pi} \right) \left( \frac{17}{2}C_F + 3C_F \log\left(\frac{\mu_R^2}{s}\right) \right) \right] \quad (2.8)$$

$$\Gamma_{H \rightarrow gg}^1(s, \mu_R) = \Gamma_{H \rightarrow gg}^0(\mu_R) \left[ 1 + \left( \frac{\alpha_s(\mu_R)}{2\pi} \right) \left( \frac{95}{6}C_A - \frac{7}{3}N_F + 2\beta_0 \log\left(\frac{\mu_R^2}{s}\right) \right) \right]. \quad (2.9)$$

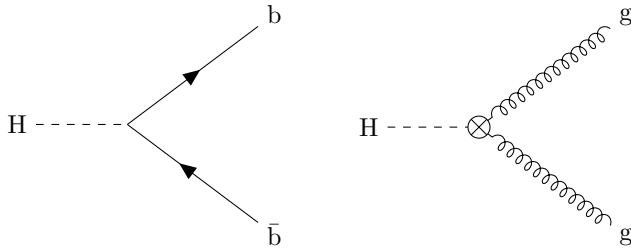


**Figure 1:** Hadronic Higgs decay categories:  $H \rightarrow b\bar{b}$  with a Yukawa coupling (*left*) and  $H \rightarrow gg$  via an effective coupling (*right*).

The rescaling factors given in eqs. (2.5) and (2.6) will be applied in section 3, where we present event-shape predictions for both decay modes.

To obtain our predictions for the Higgs event-shape distributions, we implement our NLO QCD calculation in the publicly available<sup>1</sup> EERAD3 program [56]. This code has previously been used to study event shapes [44, 45] and jet distributions [57] in  $e^+e^- \rightarrow 3j$  at NNLO. The implementation is done in a flexible manner, utilising the existing infrastructure for three-jet production in electron-positron annihilation and amending it by new subroutines for Higgs decays. All matrix elements are implemented in analytic form, enabling a fast and numerically stable evaluation of the perturbative coefficients. With this implementation, EERAD3 is promoted to a multi-process event generator, capable of calculating both off-shell  $Z/\gamma$  decays at NNLO and Higgs decays at NLO.

In the remainder of this section, we split the discussion of the ingredients of our computation in the following parts: in section 2.1, we describe the general framework in which Higgs-decay observables are computed up to NLO, while in sections 2.2 and 2.3 we present all ingredients needed in the two Higgs decay categories. We conclude in section 2.4 by explicitly summarising all checks that we have performed to confirm the correctness of our results.

## 2.1 General framework

For an infrared-safe observable  $O$ , the differential decay rate of the Higgs boson to three-jet-like final states, normalised to the respective Born-level  $H \rightarrow 2j$  decay width, can be written up to NLO in the strong coupling  $\alpha_s$  as,

$$\frac{1}{\Gamma^n(s, \mu_R)} \frac{d\Gamma(s, \mu_R, O)}{dO} = \frac{\Gamma^0(\mu_R)}{\Gamma^n(s, \mu_R)} \left( \frac{\alpha_s(\mu_R)}{2\pi} \right) \frac{dA(s)}{dO} + \frac{\Gamma^0(\mu_R)}{\Gamma^n(s, \mu_R)} \left( \frac{\alpha_s(\mu_R)}{2\pi} \right)^2 \frac{dB(s, \mu_R)}{dO}. \quad (2.10)$$

<sup>1</sup><http://eerad3.hepforge.org>

For NLO results, the differential decay rate is normalised to  $\Gamma^1$ , obtained by taking  $n = 1$  in eq. (2.10), while the additional ratios are unity for  $n = 0$ , *i.e.*, for LO results. Here,  $A$  and  $B$  denote the LO and NLO coefficients, respectively.

The LO coefficient  $A$  is determined by

$$\left(\frac{\alpha_s(\mu_R)}{2\pi}\right) \frac{dA(s)}{dO} = \frac{1}{\Gamma^0(\mu_R)} \int \frac{d\Gamma^B(s)}{d\Phi_3} \delta(O - O(\Phi_3)) d\Phi_3, \quad (2.11)$$

where  $\frac{d\Gamma^B(s)}{d\Phi_3}$  denotes the tree-level three-parton decay rate differential in the three-particle phase space. As long as  $d\Gamma^B$  contains a suitable observable definition  $\mathcal{J}_3^{(3)}(p_1, p_2, p_3)$ , which ensures that all three final-state partons are well-enough separated, the LO coefficient  $A$  is infrared-finite.

The NLO coefficient  $B$  is calculated as

$$\begin{aligned} \left(\frac{\alpha_s(\mu_R)}{2\pi}\right)^2 \frac{dB(s, \mu_R)}{dO} = & \frac{1}{\Gamma^0(\mu_R)} \int \left[ \frac{d\Gamma^V(s, \mu_R)}{d\Phi_3} + \int \frac{d\Gamma_{\text{NLO}}^T(s, \mu_R)}{d\Phi_3} \right] \delta(O - O(\Phi_3)) d\Phi_3 \\ & + \frac{1}{\Gamma^0(\mu_R)} \int \left[ \frac{d\Gamma^R(s)}{d\Phi_4} \delta(O - O(\Phi_4)) - \frac{d\Gamma_{\text{NLO}}^S(s)}{d\Phi_4} \delta(O - O(\Phi_3(\Phi_4))) \right] d\Phi_4, \end{aligned} \quad (2.12)$$

where the real and virtual subtraction terms  $d\Gamma_{\text{NLO}}^S$  and  $d\Gamma_{\text{NLO}}^T$  ensure that the real and virtual (one-loop) contributions denoted by R and V are separately infrared finite. While the real subtraction term cancels singularities in the real contribution when one parton becomes unresolved, the virtual subtraction term cancels explicit infrared singularities arising from one-loop integrals in the virtual contribution. We perform the subtraction in eq. (2.12) using the antenna-subtraction formalism [58–60]. Details on the construction of both types of subtraction terms can be found in [59].

While in principle all ingredients to our calculation are known for quite some time already, they have so far not been combined to obtain predictions for the observables considered here.

## 2.2 Yukawa-type contributions

Representative Feynman diagrams of all partonic contributions in the  $H \rightarrow b\bar{b}$  channel are shown in fig. 2, with Born-level and virtual contributions displayed in the first line and real contributions in the second line. We calculate tree-level matrix elements with up to four partons explicitly using FORM [61], taking into account all processes given in table 1. The three-parton one-loop matrix element is adapted from the real-virtual corrections of the Higgs-decay part in the NNLO VH calculation implemented in NNLOJET [38], which implements the results of [62,63]. The real NLO subtraction term has first been constructed as the single-unresolved part of the double-real subtraction term in the Higgs-decay part



**Table 1:** Partonic channels contributing to the decay  $H \rightarrow 3j$  at LO and NLO.

	$H \rightarrow b\bar{b}$ type	$H \rightarrow gg$ type	
LO	$H \rightarrow b\bar{b}g$	$H \rightarrow ggg$	tree-level
		$H \rightarrow gq\bar{q}$	tree-level
NLO	$H \rightarrow bbg$	$H \rightarrow ggg$	one-loop
		$H \rightarrow gq\bar{q}$	one-loop
	$H \rightarrow b\bar{b}gg$	$H \rightarrow gggg$	tree-level
	$H \rightarrow b\bar{b}q\bar{q}$	$H \rightarrow ggq\bar{q}$	tree-level
	$H \rightarrow b\bar{b}b\bar{b}$	$H \rightarrow q\bar{q}q'\bar{q}'$	tree-level

in [38], while the virtual NLO subtraction term corresponds to the explicit-pole part of the real-virtual subtraction contribution in that calculation.

### 2.3 Effective-theory-type contributions

Representative Feynman diagrams of all partonic contributions in the  $H \rightarrow gg$  category are shown in fig. 3, with Born-level and virtual contributions shown in the first two lines and real contributions in the third line. We construct tree-level matrix elements with up to four partons directly from gluon-gluon antenna functions [64] taking into account the processes given in table 1. The HEFT three-parton one-loop matrix elements are adapted from the MCFM  $H + 1j$  implementation [65, 66], in turn based on the results given in [67]. We note further that the  $\mathcal{O}(\alpha_s^2)$  correction to  $H \rightarrow 3j$  present in the  $H \rightarrow gg$  category at NLO receives a contribution from the  $\mathcal{O}(\alpha_s)$  expansion of the Wilson coefficient  $C(M_t, \mu_R)$  given in eq. (2.4). We implement this as a finite shift in the virtual correction

$$d\Gamma^V(s, \mu_R) \rightarrow d\Gamma^V(s, \mu_R) + 2C^{(1)}(M_t, \mu_R) \frac{\alpha_s(\mu_R)}{2\pi} d\Gamma^B(s). \quad (2.13)$$

Taking into account the crossing of the amplitudes, all HEFT one-loop amplitudes are in agreement with the respective Higgs-production one-loop matrix elements available in NNLOJET [68]. The real and virtual NLO subtraction terms for gluonic Higgs decays have first been derived in [69], based on analytic expressions for the definition of the gluon-gluon antenna functions from Higgs boson decay contained in [64].

### 2.4 Validation

To conclude this section, we elaborate on the analytical and numerical checks we performed.

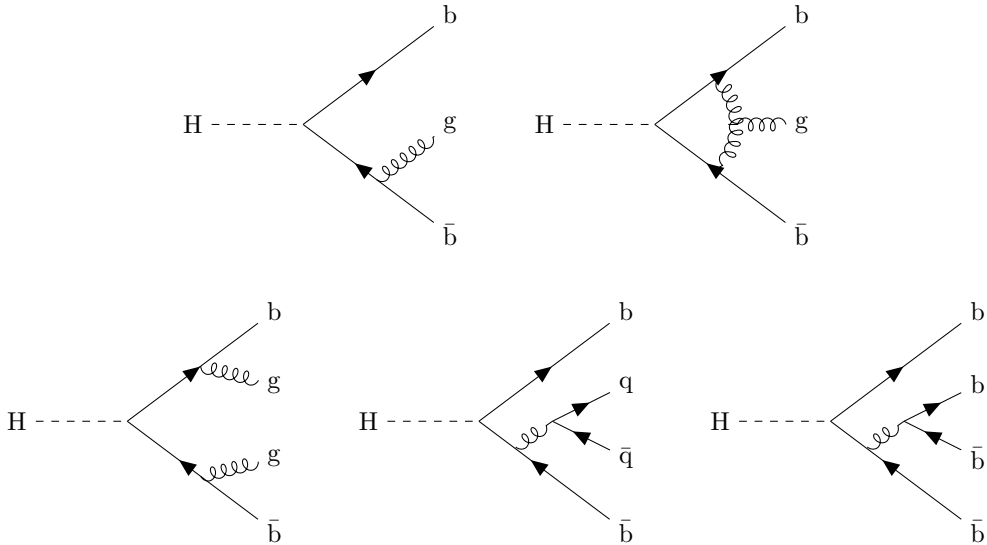


**Figure 2:** Representative Feynman diagrams for hadronic Higgs decays to bottom quarks in the  $H \rightarrow b\bar{b}$  category up to second order in  $\alpha_s$

We validated the correctness of the implementation of all matrix elements numerically on a point-by-point basis. To this end, all tree-level matrix elements have been compared against MADGRAPH5 [70, 71], the HEFT Higgs-decay one-loop matrix elements against OPENLOOPS 2 [72], and the Yukawa-induced one-loop matrix elements against POWHEG-BOX [39]. In all cases, we have found perfect agreement with the reference results up to machine precision.

Our implementation of the relevant differential NLO antenna-subtraction terms  $d\Gamma_{\text{NLO}}^{\text{S}}$  has been checked numerically on a point-by-point basis against the real correction  $d\Gamma^{\text{R}}$ . For this purpose, we have used so-called “spike-test” checks, as defined in the context of the antenna-subtraction framework for the first time in [73] and applied in the context of the NNLO di-jet computation in [74]. In all cases, we found excellent agreement between the subtraction terms and real-radiation matrix elements in the relevant single-unresolved limits. Finally, to confirm the analytic cancellation of explicit poles between virtual subtraction terms  $d\Gamma_{\text{NLO}}^{\text{T}}$  and virtual corrections  $d\Gamma^{\text{V}}$ , we have implemented numerical tests of the cancellation that are performed during actual runs.

### 3 Numerical Results

We here focus on the classical six event shape observables related to hadronic Higgs decays. Those have been studied extensively in  $e^+e^-$  collisions at LEP [75–89].

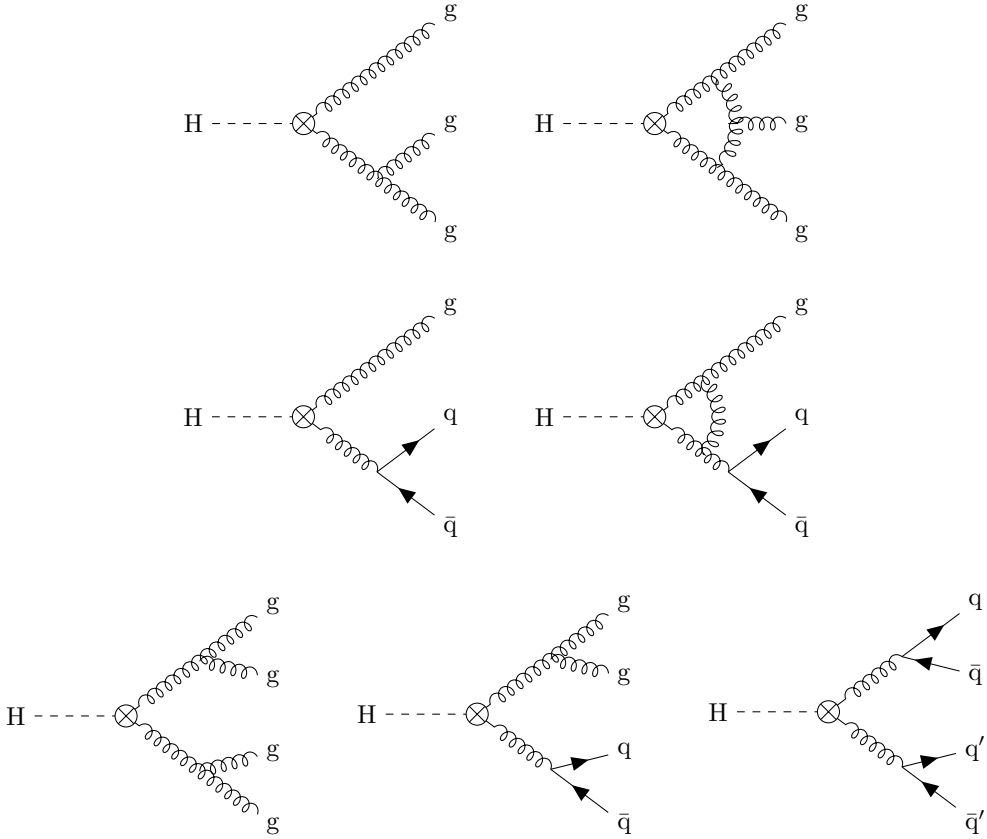


**Figure 3:** Representative Feynman diagrams for hadronic Higgs decays to gluons in the  $H \rightarrow gg$  category up to second order in  $\alpha_s$ .

After presenting the numerical set-up in section 3.1, we shall divide the discussion of our results for the six major event-shape observables into two subsections: section 3.2, where only the two Higgs decay categories are considered and section 3.3, where these predictions are also compared with those obtained for hadronic  $Z/\gamma$  decays.

### 3.1 Numerical set-up and scale-variation prescription

We consider Higgs decays with a centre-of-mass energy  $\sqrt{s} = M_H$ , equal to a Higgs mass of  $M_H = 125$  GeV. Electroweak quantities are considered as constant parameters: specifically, the electromagnetic coupling  $\alpha$  is taken to  $\alpha = \frac{1}{128}$  and the weak-boson masses to

$$M_Z = 91.1876 \text{ GeV}, \quad M_W = 80.385 \text{ GeV}. \quad (3.1)$$

For the QCD part, all quantities are renormalisation-scale dependent and a scale-variation prescription is applied. The renormalisation scale  $\mu_R$  is varied as a multiple

$\mu_R \rightarrow k_\mu \mu_R$  with  $k_\mu \in [\frac{1}{2}, 2]$  of the on-shell Higgs-boson mass  $M_H$ , which we choose as our central scale,  $\mu_R = M_H$ . We use a one and two-loop running for the strong coupling  $\alpha_s$ , at LO and NLO respectively, with a nominal value at scale  $M_Z$  given by  $\alpha_s(M_Z) = 0.1189$ . The former is obtained by solving the renormalisation-group equation at the given order, as detailed in [44, 56].

Further, throughout the computation, we keep a vanishing kinematical mass of the b-quark, but consider a non-vanishing Yukawa mass. We calculate the latter using the result of [55], corresponding to  $\bar{m}_b(M_H)$  close to 2.61 GeV.

Fixed-order calculations of event shapes are generically only valid away from the two-jet limit, as they obtain large logarithmic corrections of the form  $\alpha_s^n L^n$ , where  $L \sim \log(1/O)$ , when additional particles become unresolved [90]. In order to obtain reliable predictions in the two-jet region, these logarithms have to be resummed, *cf. e.g.* [91–94] for the combination of fixed-order and resummed predictions for event shapes in  $e^+e^-$  annihilation. As a consequence, we therefore impose a small cut-off  $y_0 = 10^{-5}$  on all linear distributions and  $y_0 = e^{-10}$  on logarithmically binned distributions in practice.

### 3.2 Differential predictions for Higgs-decay event-shape observables

We here collect LO and NLO predictions for all six classical event shapes in figs. 4 to 6, where we present observable-weighted distributions of the form,

$$\frac{\text{Br}^n(s, \mu_R)}{\Gamma^n(s, \mu_R)} O \frac{d\Gamma(s, \mu_R, O)}{dO}. \quad (3.2)$$

More specifically, according to eq. (3.2), these normalised differential decay rates, given in eq. (2.10) are multiplied by the event-shape observable itself and scaled by the corresponding fixed-order branching ratio of the respective Higgs-decay category as given in eqs. (2.5) and (2.6):

$$\text{Br}_{H \rightarrow b\bar{b}}^0(s = M_H^2, M_H) \approx 0.933, \quad \text{Br}_{H \rightarrow gg}^0(s = M_H^2, M_H) \approx 0.067, \quad (3.3)$$

$$\text{Br}_{H \rightarrow b\bar{b}}^1(s = M_H^2, M_H) \approx 0.908, \quad \text{Br}_{H \rightarrow gg}^1(s = M_H^2, M_H) \approx 0.092. \quad (3.4)$$

We have checked that the relative size of the  $H \rightarrow gg$  and  $H \rightarrow b\bar{b}$  branching ratios in eqs. (3.3) and (3.4) is in line with the results of [95].

In general, each of the figures, numbered as figs. 4 to 6, are composed of four panels: the upper panel contains the distributions, while the lower three panels contain three ratios evaluated using differential results from the  $H \rightarrow gg$  decay category in the numerator results from the  $H \rightarrow b\bar{b}$  decay category in the denominator. The first ratio panel contains both LO and NLO results, while the second and third panel zoom in on the LO and NLO results,

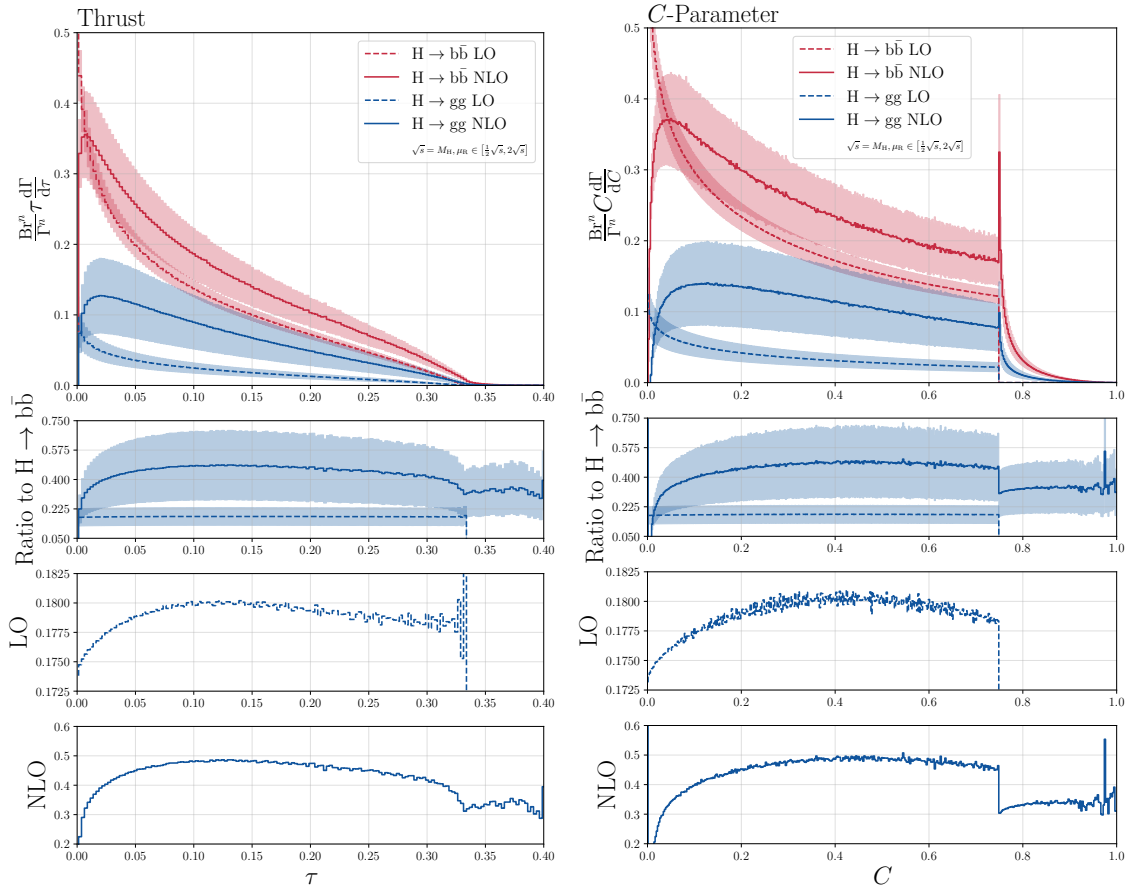


**Figure 4:** Thrust (*left*) and  $C$ -parameter (*right*). The upper panel contains predictions in the  $H \rightarrow gg$  (*blue*) and  $H \rightarrow b\bar{b}$  (*red*) categories at LO (*dashed*) and NLO (*solid*), with renormalisation-scale uncertainties shown as light-shaded bands. The three lower panels show bin-by-bin ratios at LO and NLO, see main text.

respectively. The line colour and style in the upper panel is chosen as follows:  $H \rightarrow b\bar{b}$  is shown in red,  $H \rightarrow gg$  in blue; NLO results have solid lines, and LO results have dashed lines. In the lower panels, all ratio histograms inherit the colour of the numerator. Those are therefore all shown in blue. Uncertainties arising from a variation of the renormalisation scale in the aforementioned envelope  $\mu_R \in [\frac{1}{2}\sqrt{s}, 2\sqrt{s}]$  are shown as light-shaded bands around the central results. For the sake of clarity, uncertainty bands are only shown in the upper panel and in the joint (second panel) showing both LO and NLO ratios.

As can be inferred from the relative size of the branching ratios given in eqs. (3.3) and (3.4), it is found that the  $H \rightarrow b\bar{b}$  decay part is the dominant one in all distributions. We observe sizeable NLO corrections in both the di-gluon and the b-quark decay channel, with generally significantly larger corrections in the former. In all cases, renormalisation-

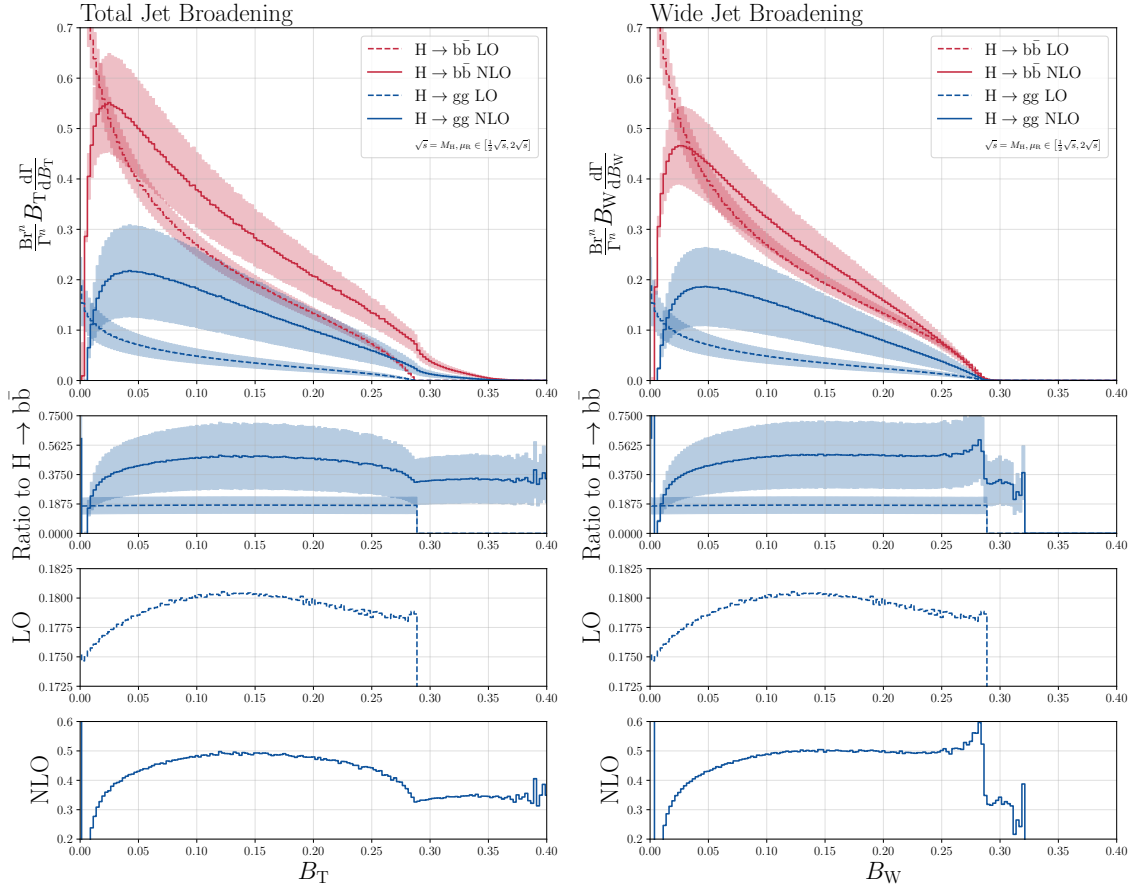


**Figure 5:** Total (*left*) and wide jet broadening (*right*). The upper panel contains predictions in the  $H \rightarrow gg$  (*blue*) and  $H \rightarrow b\bar{b}$  (*red*) categories at LO (*dashed*) and NLO (*solid*), with renormalisation-scale uncertainties shown as light-shaded bands. The three lower panels show bin-by-bin ratios at LO and NLO, see main text.

scale uncertainties are comparatively large at NLO, indicating that NNLO corrections can be expected to be non-negligible. Our findings regarding the large size of NLO corrections in the di-gluon channel is not unexpected. A similar behaviour is observed in Higgs production in gluon-gluon fusion, where at least NNLO corrections are mandatory to obtain precise predictions, as first calculated in [96]. All distributions develop the expected perturbative properties that the differential cross sections diverge in the two-jet limit towards positive infinity at LO, while at NLO, they turn towards negative infinity. As a consequence, all distributions show the characteristic extremum towards the infrared region.

For all event-shape distributions considered here, the differential ratio of the  $H \rightarrow gg$  to the  $H \rightarrow b\bar{b}$  result varies around 17.5% – 18.0% at LO and around 30% – 50% at NLO. A very distinctive feature is also that at LO level, the ratio between the  $H \rightarrow gg$  and

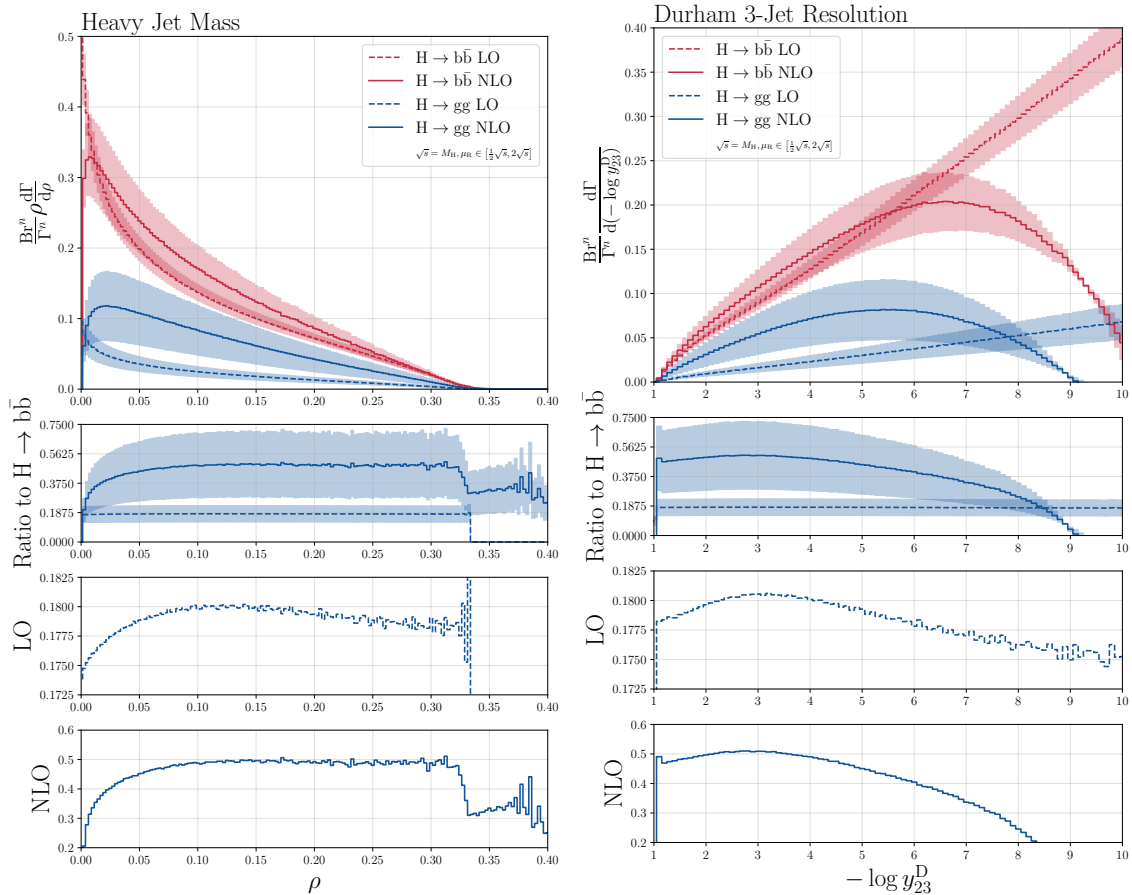


**Figure 6:** Heavy-jet mass (*left*) and Durham three-jet resolution (*right*). The upper panel contains predictions in the  $H \rightarrow gg$  (*blue*) and  $H \rightarrow b\bar{b}$  (*red*) categories at LO (*dashed*) and NLO (*solid*), with renormalisation-scale uncertainties shown as light-shaded bands. The three lower panels show bin-by-bin ratios at LO and NLO, see main text.

$H \rightarrow b\bar{b}$  channels always develops an insignificant, seemingly constant shape with a plateau towards the multi-jet limit. While the LO ratio shapes can be highlighted on a zoomed-in scale, these are overwhelmed by the size of the NLO corrections. In particular, this implies that the discriminative power of event shapes is significantly reduced if no higher-order corrections are taken into account, either via fixed-order corrections or (parton-shower) resummation. In all cases, the shape of the ratio distribution at NLO resembles the LO one, however, significantly amplified and with shape differences towards the multi-jet limit. Below, we will therefore limit the discussion to the results associated to each of the six event shape observables at NLO level.

**Thrust** For multi-jet final states in lepton collisions, the thrust is defined as [97, 98]

$$T = \max_{\vec{n}} \left( \frac{\sum_i |\vec{p}_i \cdot \vec{n}|}{\sum_i |\vec{p}_i|} \right), \quad (3.5)$$

where the sum of three-momenta is maximised over the direction of  $\vec{n}$ . The unit vector  $\vec{n}_T$  which maximises the expression on the right-hand side defines the thrust axis. For two-jet events, the thrust approaches unity,  $T \rightarrow 1$ , while for three-jet events  $T \geq \frac{2}{3}$ . In practice, we consider the observable  $\tau = 1 - T$ , so that  $\tau > 0$  measures the departure from a two-particle topology.

The thrust distributions are shown in the left-hand panel of fig. 4. In the region  $0.05 \leq \tau \leq 0.25$ , we find differential NLO  $K$ -factors varying in the range 1.29 – 1.53 in the  $H \rightarrow b\bar{b}$  decay category and between 3.2 and 3.84 in the  $H \rightarrow gg$  category.

Our results are in agreement with the NLO results presented in [47]. Furthermore, we have implemented the analytic expressions provided in [47] for both Higgs decay categories and found perfect agreement with our corresponding numerical results.

Our NLO predictions for the thrust distribution have the following features: as shown in the left-hand panel of fig. 4, for the di-gluon channel, the peak of the distribution is slightly shifted towards the hard region on the right-hand side of the plot. Moreover, the distribution is broader in the  $H \rightarrow gg$  channel, as is visible from the ratio plots in the lower panes of the figure. Despite generally looking rather flat above  $\tau \approx 0.05$ , the ratio to the  $b\bar{b}$  channel reaches a maximum at  $\tau = 0.1 - 0.15$  and slowly falls off after. While only developing a small shape difference in the intermediate  $\tau$  region, the thrust distribution may therefore offer some potential for discriminating the Higgs-decay processes involving either heavy quarks or gluons, if this particular kinematical region is enhanced by suitably placed cuts.

**$C$ -Parameter** The  $C$ -parameter,

$$C = 3(\lambda_1\lambda_2 + \lambda_2\lambda_3 + \lambda_3\lambda_1), \quad (3.6)$$

is defined in terms of the three eigenvalues  $\lambda_{1,2,3}$  of the linearised momentum tensor [99, 100]

$$\Theta^{\alpha\beta} = \frac{1}{\sum_j |\vec{p}_j|} \sum_j \frac{p_j^\alpha p_j^\beta}{|\vec{p}_j|}, \text{ where } \alpha, \beta \in \{1, 2, 3\}. \quad (3.7)$$

Results for the  $C$ -parameter are presented in the right-hand pane of fig. 4. Clearly visible in both decay categories is the characteristic Sudakov shoulder [101] around  $C \approx$



0.75, where large logarithms in the physical region spoil the convergence of fixed-order calculations. In the region  $0.1 \leq C \leq 0.6$ , we find differential NLO  $K$ -factors ranging from 1.17 – 1.40 in the  $H \rightarrow b\bar{b}$  decay category and from 2.61 – 3.84 in the  $H \rightarrow gg$  category.

As for the thrust, the peak of the distribution is shifted towards the hard region on the right-hand side of the plot in the di-gluon channel. It is to be noted, however, that the ratio plots differ considerably compared to the thrust case. The ratio to the b-quark channel distribution levels at values  $C \gtrsim 0.2$ , which limits the applicability of the  $C$ -parameter as a good observable for distinguishing the two Higgs-decay processes.

**Jet Broadening** The total and wide jet broadening  $B_T$  and  $B_W$  are defined by [102, 103]

$$B_T = B_1 + B_2 \quad B_W = \max(B_1, B_2), \quad (3.8)$$

in terms of the hemisphere broadening

$$B_i = \frac{\sum_{j \in H_i} |\vec{p}_i \times \vec{n}_T|}{2 \sum_j |\vec{p}_j|}, \quad (3.9)$$

for two hemispheres  $H_{1,2}$  separated by the thrust vector  $\vec{n}_T$ . Both vanish in the two-jet limit,  $B_T \rightarrow 0$ ,  $B_W \rightarrow 0$ , and are bounded from above by  $B_T = B_W = \frac{1}{2\sqrt{3}}$ .

The jet-broadening distributions are shown in fig. 5. Expectedly, both distributions have discontinuities at the three-jet maximum  $\frac{1}{2\sqrt{3}} \approx 0.29$ , where the NLO calculation receives new contributions from four-particle configurations. The NLO corrections are generically smaller for the wide jet broadening than for the total jet broadening. Specifically, for the total jet broadening, we find differential NLO  $K$ -factors of around 1.25 – 1.55 in the  $H \rightarrow b\bar{b}$  decay category and around 2.99 – 4.13 in the  $H \rightarrow gg$  category in the region  $0.05 \leq B_T \leq 0.2$ . For the wide jet broadening, we find differential NLO  $K$ -factors of around 1.06 – 1.24 in the  $H \rightarrow b\bar{b}$  decay category and 2.58 – 3.44 in the  $H \rightarrow gg$  category in the region  $0.05 \leq B_W \leq 0.25$ .

The ratio of the total-jet-broadening distributions develops a broad, however peaked, structure with a maximum around  $B_T \approx 0.15$ , whereas the ratio in the case of the wide jet broadening distribution grows monotonically with a sharp peak at around  $B_W \approx 0.28$  and an inflection at around  $B_W \approx 0.15$ . While the sharp peak in the wide-jet-broadening ratio plot may be considered useful for discrimination applications, it has to be noted that it lies in a region where higher-order corrections from fixed-order or resummed calculations have a large impact. In combination with the fact that this sharp peak is followed by a discontinuity (which vanishes upon resummation), we conclude that the wide jet broadening is not a suitable candidate for discrimination of Higgs decays to bottom quark pairs or

gluons, because of the overall flat ratio between the two decay categories above  $B_W \approx 0.1$ . The total jet broadening, on the other hand, shows a similar shape difference between the two decay channels as the thrust distribution. As such, it may offer some potential to be used as a good discriminator if the region  $0.05 \leq B_T \leq 0.25$  can be suitably enhanced via well-placed cuts.

**Heavy-jet mass** In order to define the heavy-jet (or heavy-hemisphere) mass, the event is divided into two hemispheres  $H_1, H_2$ , for each of which the scaled invariant mass is calculated [104]:

$$\frac{M_i^2}{s} = \frac{1}{E_{\text{vis}}^2} \left( \sum_{j \in H_i} p_j \right)^2. \quad (3.10)$$

We define the two hemispheres so that they are separated by a plane orthogonal to the thrust axis and calculate the heavy-jet mass as the maximum over the two invariant masses,

$$\rho = \max_{i \in \{1,2\}} \left( \frac{M_i}{s} \right) \equiv \frac{M_H^2}{s}. \quad (3.11)$$

The  $\rho$  and  $\tau$  distributions are identical at LO and as such vanish in the two-particle limit,  $\rho \rightarrow 0$ . For three-jet events, the heavy-jet mass is bounded by  $\rho \leq \frac{1}{3}$ .

The left-hand plot in fig. 6 contains the heavy-jet mass distributions in both Higgs-decay channels. In the region  $0.05 \leq \rho \leq 0.25$ , we find comparatively modest differential NLO  $K$ -factors of about 1.14 – 1.26 in the  $H \rightarrow b\bar{b}$  decay category and 2.99 – 3.44 in the  $H \rightarrow gg$  category.

The ratio of the distributions obtained in the two categories remains almost exactly constant above  $\rho \approx 0.1$ , heavily limiting its application for disentangling the two Higgs-decay processes, as virtually no shape difference can be determined in the region  $0.05 \leq \rho \leq 0.3$  in which the fixed-order calculation can be trusted.

**3-Jet Resolution** For a given jet algorithm, the three-jet resolution variable is given by that value for which an event is clustered from a three-jet event to a two-jet event. In particular, we consider here the Durham jet algorithm, using the particle-distance measure [105–109]

$$y_{ij}^D = \frac{2 \min(E_i^2, E_j^2)(1 - \cos \theta_{ij})}{E_{\text{vis}}^2}, \quad (3.12)$$

for each particle pair  $(i, j)$ . In the so-called “E-scheme”, the pair with smallest resolution  $y_{ij}^D$  is replaced by a pseudo-particle with a four-momentum equal to the sum of the four-momenta of  $i$  and  $j$  at each step of the jet algorithm. As long as there are pairs with invariant mass below a cut  $y_{\text{cut}}$  in the event, this procedure is repeated.

The three-jet resolution scale in the Durham algorithm is shown in the right-hand part of fig. 6. In the region  $2 \leq -\log(y_{23}^D) \leq 5$ , we find modest differential NLO  $K$ -factors of about 1.07 – 1.21 in the  $H \rightarrow b\bar{b}$  decay category and 2.71 – 3.39 in the  $H \rightarrow gg$  category.

In comparison to the previously discussed event-shape distributions, the three-jet clustering scale shows a slightly more complex shape difference between the di-gluon and quark-pair channel. While the peak of the  $H \rightarrow b\bar{b}$  distribution is located at around  $\log y_{23}^D \approx -6.5$ , it is shifted to  $\log y_{23}^D \approx -5.5$  for the  $H \rightarrow gg$  case. Moreover, the latter has a higher rate towards the hard region at the left-hand side of the plot, implying that gluon-induced jets are typically clustered earlier (at higher resolution scales) than quark-induced ones. This excess of gluon-induced jet clusterings is most pronounced at around  $\log y_{23}^D \approx -3$ , as is visible from the first ratio panel in fig. 6. In this phase-space region, the three-jet resolution parameter may therefore prove itself useful for disentangling Higgs decays related to bottom quark pairs and gluons.

**Summary** In conclusion, the event shapes studied here can be classified into two classes. We classify the observables depending on whether the ratio between the  $H \rightarrow gg$  and  $H \rightarrow b\bar{b}$  result forms a plateau in the multi-jet limit or develops a maximum at intermediate event-shape values. While the former class offers virtually no potential for separating the contributions coming from Higgs decays to bottom quark pairs and gluons, the latter class is more suited towards this application due its richer structure. Event shapes falling into the first class are the  $C$ -parameter, wide jet broadening, and the heavy-jet mass; event shapes of the second class are thrust, total jet broadening, and the Durham three-jet scale, *cf.* figs. 4 to 6.

### 3.3 Comparison to $(Z/\gamma)^*$ decays

To further gauge the discriminatory power of event shapes, in fig. 7 we compare the event-shape distributions in hadronic Higgs decays to the distributions associated to off-shell photon/ $Z$  decays as originally implemented in EERAD3 [44,45,56]. To this end, we choose the same setup as in section 3.1, with a centre-of-mass energy of  $\sqrt{s} = M_H$ . The results are shown in fig. 7, consisting of two panels: the upper panel contains the  $H \rightarrow gg$ ,  $H \rightarrow b\bar{b}$ , and  $(Z/\gamma)^* \rightarrow q\bar{q}$  distributions at NLO, while the lower panel shows the ratio of the sum of the two Higgs-decay distributions to the off-shell photon/ $Z$  distributions at NLO level. We again show  $H \rightarrow b\bar{b}$  results in red and  $H \rightarrow gg$  results in blue; in addition, results for  $(Z/\gamma)^* \rightarrow q\bar{q}$  distributions are shown in green and inclusive H-decay distributions (*i.e.* the sum of the two categories) are plotted in purple.

Notwithstanding normalisation differences, the  $(Z/\gamma)^* \rightarrow q\bar{q}$  distributions resemble

closely the  $H \rightarrow b\bar{b}$  ones, with some small shape differences. Compared to the shape difference to the distributions in the  $H \rightarrow gg$  category, however, these are only minor. The exception here seems to be the  $C$ -parameter, where the difference between the quark-induced Higgs decay and the off-shell photon/ $Z$  decay is more pronounced. Nevertheless, all quark-induced  $(Z/\gamma)^* \rightarrow q\bar{q}$  and  $H \rightarrow b\bar{b}$  distributions peak at roughly equal event-shape values, whereas the peak is considerably shifted for the gluon-induced channel  $H \rightarrow gg$ . This is visible from the upper panel of fig. 7, where the maxima in the Higgs-decay distributions have been marked by coloured dashed lines. This observation is in line with expectations, as higher-order corrections are expected in the region towards the right-hand side of the plots and resummation of large logarithms is necessary in the two-jet limit on the left edge of the linearly binned histograms.

In particular, in the logarithmically binned  $y_{23}^D$  distribution, rather good agreement in the shape of the two quark-induced distributions is found in the region  $\log y_{23}^D \geq -4$ , with some deviations observed in the region  $\log y_{23}^D < -4$ , with a slight shift of the maximum of the  $(Z/\gamma)^* \rightarrow q\bar{q}$  distribution towards larger clustering scales. The  $H \rightarrow gg$  distribution, on the other hand, is visibly more narrow with a peak located much closer to the hard phase-space region.

The ratio of the inclusive hadronic Higgs-decay distributions, given by the sum of the individual  $H \rightarrow gg$  and  $H \rightarrow b\bar{b}$  distributions, to the off-shell  $(Z/\gamma)$ -decay result is shown as a dark purple line in the ratio panels of the figures in fig. 7. In all six event-shape distributions, this ratio shows a clear trend, namely that it is an almost linear distribution up to the three-parton kinematical limit. In particular, the combined Higgs-decay distributions all show a significantly higher rate towards the multi-jet limit. In the case of the Durham three-jet resolution, shown in the lower right-hand pane in fig. 7, this straight-forwardly translates into the presence of larger clustering scales for hadronic Higgs decays than for hadronic  $Z/\gamma$ -decays.

It is also worth noting that scale uncertainties in the Higgs-decay results are generally larger than for the  $(Z/\gamma)^*$  decay. This is partly due to the additional branching-ratio prefactors  $\text{Br}^n$  in eq. (3.2), which need to be taken into account in the scale-variation prescription to ensure consistency with the  $\Gamma^n$  normalisation. While a variation of the  $H \rightarrow gg$  and  $H \rightarrow b\bar{b}$  branching ratios introduces notable shifts in the relative size of the distributions, this additional shift is absent for off-shell photon/ $Z$  decays, where only a single decay category contributes. Note further that the scale uncertainties on the event shapes related to the  $H \rightarrow gg$  category are already larger per se, due to their larger NLO corrections, as already mentioned in 3.2.

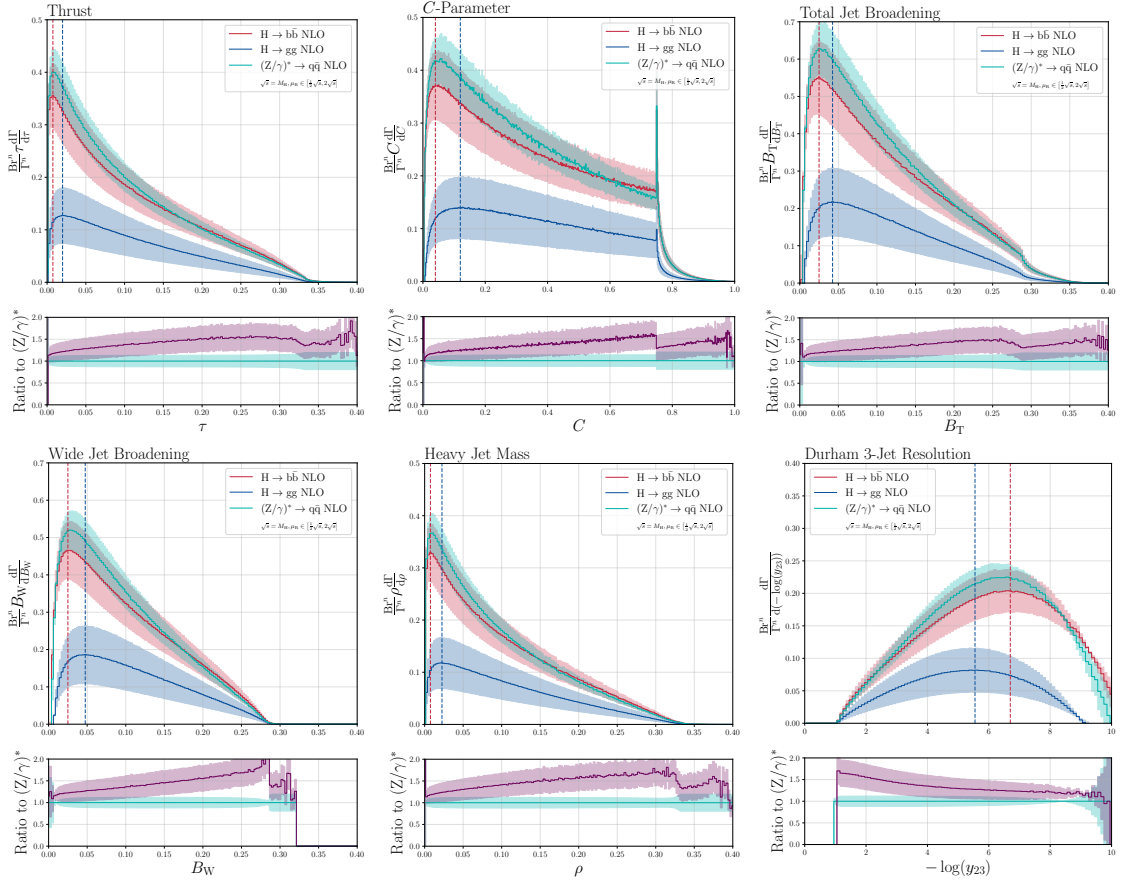


**Figure 7:** Comparison of event-shape distributions in hadronic Higgs decays and off-shell photon/ $Z$  decays. In the upper panel, the maxima of the  $H \rightarrow b\bar{b}$  and  $H \rightarrow gg$  distributions are marked with dashed red and blue lines, respectively (see text). In the lower panel, the ratio of the Higgs-decay result summed over the two categories is shown with respect to the respective  $(Z/\gamma)^*$ -decay results.

Most importantly, the comparison to results in  $(Z/\gamma)^* \rightarrow q\bar{q}$  decays confirms our assessment that visible shape differences in the intermediate regions of the  $H \rightarrow b\bar{b}$  and  $H \rightarrow gg$  distributions are primarily rooted in the distinct quark and gluon radiation patterns and may as such assist in the discrimination of Higgs decays to heavy quarks and gluons.

## 4 Summary and Outlook

In this paper, we have, for the first time, presented a full-fledged NLO calculation of all six classical event-shape observables in hadronic Higgs decays involving three parton final states at Born level. The latter supplements an earlier NLO calculation of the thrust observable (as presented in [47]), by the  $C$ -parameter, the total and wide jet broadening,

the heavy-jet mass, and the Durham three-jet resolution event shapes.

Using the antenna-subtraction framework, we have extended the existing EERAD3 NNLO parton-level Monte Carlo generator to compute hadronic Higgs-decay event shapes at NLO level. We have shown that all Higgs event-shape distributions have large NLO corrections, with more important corrections found in the di-gluon induced case. Specifically, differential  $K$ -factors lie between  $1.07 - 1.55$  in the  $H \rightarrow b\bar{b}$  decay mode, while being around  $2.58 - 4.13$  in the  $H \rightarrow gg$  mode, with different shapes and magnitudes for different event-shape distributions. We demonstrated that at NLO, different event-shape observables develop different shapes between the two Higgs decay categories and discussed the resulting applicability to discrimination purposes. In particular, for all observables, at LO, we find that the ratio is rather flat around  $17.5\% - 18\%$ , while at NLO, the ratio is amplified both in size and shape and lies around  $30\% - 50\%$ . For the specific cases, we conclude that the  $C$ -parameter, the wide jet broadening, and the heavy-jet mass have no or very limited potential as Higgs decay class discriminators, while the thrust and the total jet broadening can be considered as suitable candidates for this purpose. Of all six event shapes studied in this work, the Durham three-jet resolution shows the best potential to accomplish this disentanglement, due to a notable difference in the clustering scales between quark- and gluon-induced jets. We have verified our assessment by comparing event shapes in hadronic Higgs decays to event shapes in hadronic off-shell photon/ $Z$  decays. In all event-shape distributions, this comparison indicated a clear shift of the peaks away from the two-jet limit for gluon-induced decays.

We observe large scale uncertainties at NLO, suggesting potentially sizeable NNLO corrections specially in the  $H \rightarrow gg$  category. The inclusion of second-order QCD corrections in the present computation leading to an extension of the validity of the theoretical predictions for Higgs decays to NNLO accuracy as well as the combination with Higgs production at lepton and hadron colliders is facilitated by the flexibility of the current implementation.

Since fixed-order calculations of event-shape observables are trustworthy only in a limited phase-space region, it is furthermore expedient to consider the resummation of logarithmically enhanced contributions, be it via the combination with analytic calculations or the matching to parton showers, *cf.* [110, 111]. While the former gives an accurate account of the enhanced (next-to-)next-to-leading logarithmic contributions, the latter allows for particle-level corrections such as hadronisation. Both of these possible extensions are left for future work.

## Acknowledgments

We thank John Campbell and Imre Majer for helpful comments on the implementations of Higgs-decay one-loop matrix elements in MCFM and NNLOJET, respectively, and Thomas Gehrmann for useful discussions. This research is supported by the Swiss National Science Foundation (SNF) under contract 200021-197130 and by the Swiss National Supercomputing Centre (CSCS) under project ID ETH5f.

## References

- [1] **ATLAS** Collaboration, G. Aad et al., *Observation of a new particle in the search for the Standard Model Higgs boson with the ATLAS detector at the LHC*, *Phys. Lett. B* **716** (2012) 1–29, [[arXiv:1207.7214](#)].
- [2] **CMS** Collaboration, S. Chatrchyan et al., *Observation of a New Boson at a Mass of 125 GeV with the CMS Experiment at the LHC*, *Phys. Lett. B* **716** (2012) 30–61, [[arXiv:1207.7235](#)].
- [3] **LHC Higgs Cross Section Working Group** Collaboration, D. de Florian et al., *Handbook of LHC Higgs Cross Sections: 4. Deciphering the Nature of the Higgs Sector*, [arXiv:1610.07922](#).
- [4] M. Cepeda et al., *Report from Working Group 2: Higgs Physics at the HL-LHC and HE-LHC*, *CERN Yellow Rep. Monogr.* **7** (2019) 221–584, [[arXiv:1902.00134](#)].
- [5] **FCC** Collaboration, A. Abada et al., *FCC-ee: The Lepton Collider: Future Circular Collider Conceptual Design Report Volume 2*, *Eur. Phys. J. ST* **228** (2019), no. 2 261–623.
- [6] A. Arbey et al., *Physics at the  $e^+e^-$  Linear Collider*, *Eur. Phys. J. C* **75** (2015), no. 8 371, [[arXiv:1504.01726](#)].
- [7] **CEPC Study Group** Collaboration, M. Dong et al., *CEPC Conceptual Design Report: Volume 2 - Physics & Detector*, [arXiv:1811.10545](#).
- [8] *The International Linear Collider Technical Design Report - Volume 2: Physics*, [arXiv:1306.6352](#).
- [9] **ATLAS** Collaboration, M. Aaboud et al., *Observation of  $H \rightarrow b\bar{b}$  decays and  $VH$  production with the ATLAS detector*, *Phys. Lett. B* **786** (2018) 59–86, [[arXiv:1808.08238](#)].
- [10] **CMS** Collaboration, A. M. Sirunyan et al., *Observation of Higgs boson decay to bottom quarks*, *Phys. Rev. Lett.* **121** (2018), no. 12 121801, [[arXiv:1808.08242](#)].

- [11] P. Gras, S. Höche, D. Kar, A. Larkoski, L. Lönnblad, S. Plätzer, A. Siódmok, P. Skands, G. Soyez, and J. Thaler, *Systematics of quark/gluon tagging*, *JHEP* **07** (2017) 091, [[arXiv:1704.03878](#)].
- [12] J. Mo, F. J. Tackmann, and W. J. Waalewijn, *A case study of quark-gluon discrimination at NNLL' in comparison to parton showers*, *Eur. Phys. J. C* **77** (2017), no. 11 770, [[arXiv:1708.00867](#)].
- [13] L. Cavallini, A. Coccaro, C. K. Khosa, G. Manco, S. Marzani, F. Parodi, D. Rebutti, A. Rescia, and G. Stagnitto, *Tagging the Higgs boson decay to bottom quarks with colour-sensitive observables and the Lund jet plane*, [arXiv:2112.09650](#).
- [14] F. Dreyer, G. Soyez, and A. Takacs, *Quarks and gluons in the Lund plane*, [arXiv:2112.09140](#).
- [15] O. Fedkevych, C. K. Khosa, S. Marzani, and F. Sforza, *Identification of b-jets using QCD-inspired observables*, [arXiv:2202.05082](#).
- [16] S. G. Gorishnii, A. L. Kataev, S. A. Larin, and L. R. Surguladze, *Corrected three-loop QCD correction to the correlator of the quark scalar currents and  $\Gamma_{\text{Tot}}(H^0 \rightarrow \text{hadrons})$* , *Mod. Phys. Lett. A* **5** (1990) 2703–2712.
- [17] S. G. Gorishnii, A. L. Kataev, S. A. Larin, and L. R. Surguladze, *Scheme dependence of the next-to-next-to-leading QCD corrections to  $\Gamma_{\text{Tot}}(H^0 \rightarrow \text{hadrons})$  and the spurious QCD infrared fixed point*, *Phys. Rev. D* **43** (1991) 1633–1640.
- [18] A. L. Kataev and V. T. Kim, *The Effects of the QCD corrections to  $\Gamma(H^0 \rightarrow b\bar{b})$* , *Mod. Phys. Lett. A* **9** (1994) 1309–1326.
- [19] L. R. Surguladze, *Quark mass effects in fermionic decays of the Higgs boson in  $O(\alpha_s^2)$  perturbative QCD*, *Phys. Lett. B* **341** (1994) 60–72, [[hep-ph/9405325](#)].
- [20] S. A. Larin, T. van Ritbergen, and J. A. M. Vermaseren, *The Large top quark mass expansion for Higgs boson decays into bottom quarks and into gluons*, *Phys. Lett. B* **362** (1995) 134–140, [[hep-ph/9506465](#)].
- [21] K. G. Chetyrkin and A. Kwiatkowski, *Second order QCD corrections to scalar and pseudoscalar Higgs decays into massive bottom quarks*, *Nucl. Phys. B* **461** (1996) 3–18, [[hep-ph/9505358](#)].
- [22] K. G. Chetyrkin, *Correlator of the quark scalar currents and  $\Gamma_{\text{Tot}}(H \rightarrow \text{hadrons})$  at  $O(\alpha_s^3)$  in pQCD*, *Phys. Lett. B* **390** (1997) 309–317, [[hep-ph/9608318](#)].
- [23] P. A. Baikov, K. G. Chetyrkin, and J. H. Kuhn, *Scalar correlator at  $O(\alpha_s^4)$ , Higgs decay into b-quarks and bounds on the light quark masses*, *Phys. Rev. Lett.* **96** (2006) 012003, [[hep-ph/0511063](#)].



- [24] M. Spira, A. Djouadi, D. Graudenz, and P. M. Zerwas, *Higgs boson production at the LHC*, *Nucl. Phys. B* **453** (1995) 17–82, [[hep-ph/9504378](#)].
- [25] T. Inami, T. Kubota, and Y. Okada, *Effective Gauge Theory and the Effect of Heavy Quarks in Higgs Boson Decays*, *Z. Phys. C* **18** (1983) 69–80.
- [26] K. G. Chetyrkin, B. A. Kniehl, and M. Steinhauser, *Hadronic Higgs decay to order  $\alpha_s^4$* , *Phys. Rev. Lett.* **79** (1997) 353–356, [[hep-ph/9705240](#)].
- [27] P. A. Baikov and K. G. Chetyrkin, *Top Quark Mediated Higgs Boson Decay into Hadrons to Order  $\alpha_s^5$* , *Phys. Rev. Lett.* **97** (2006) 061803, [[hep-ph/0604194](#)].
- [28] J. Fleischer and F. Jegerlehner, *Radiative Corrections to Higgs Decays in the Extended Weinberg-Salam Model*, *Phys. Rev. D* **23** (1981) 2001–2026.
- [29] D. Y. Bardin, B. M. Vilensky, and P. K. Khristova, *Calculation of the Higgs boson decay width into fermion pairs*, *Sov. J. Nucl. Phys.* **53** (1991) 152–158.
- [30] A. Dabelstein and W. Hollik, *Electroweak corrections to the fermionic decay width of the standard Higgs boson*, *Z. Phys. C* **53** (1992) 507–516.
- [31] B. A. Kniehl, *Radiative corrections for  $H \rightarrow f\bar{f}(\gamma)$  in the standard model*, *Nucl. Phys. B* **376** (1992) 3–28.
- [32] U. Aglietti, R. Bonciani, G. Degrassi, and A. Vicini, *Two loop light fermion contribution to Higgs production and decays*, *Phys. Lett. B* **595** (2004) 432–441, [[hep-ph/0404071](#)].
- [33] G. Degrassi and F. Maltoni, *Two-loop electroweak corrections to Higgs production at hadron colliders*, *Phys. Lett. B* **600** (2004) 255–260, [[hep-ph/0407249](#)].
- [34] S. Actis, G. Passarino, C. Sturm, and S. Uccirati, *NLO Electroweak Corrections to Higgs Boson Production at Hadron Colliders*, *Phys. Lett. B* **670** (2008) 12–17, [[arXiv:0809.1301](#)].
- [35] U. Aglietti, R. Bonciani, G. Degrassi, and A. Vicini, *Master integrals for the two-loop light fermion contributions to  $gg \rightarrow H$  and  $H \rightarrow \gamma\gamma$* , *Phys. Lett. B* **600** (2004) 57–64, [[hep-ph/0407162](#)].
- [36] G. Ferrera, G. Somogyi, and F. Tramontano, *Associated production of a Higgs boson decaying into bottom quarks at the LHC in full NNLO QCD*, *Phys. Lett. B* **780** (2018) 346–351, [[arXiv:1705.10304](#)].
- [37] F. Caola, G. Luisoni, K. Melnikov, and R. Röntsch, *NNLO QCD corrections to associated  $WH$  production and  $H \rightarrow b\bar{b}$  decay*, *Phys. Rev. D* **97** (2018), no. 7 074022, [[arXiv:1712.06954](#)].

- [38] R. Gauld, A. Gehrmann-De Ridder, E. W. N. Glover, A. Huss, and I. Majer, *Associated production of a Higgs boson decaying into bottom quarks and a weak vector boson decaying leptonically at NNLO in QCD*, *JHEP* **10** (2019) 002, [[arXiv:1907.05836](#)].
- [39] W. Bizoń, E. Re, and G. Zanderighi, *NNLOPS description of the  $H \rightarrow b\bar{b}$  decay with  $MinLO$* , *JHEP* **06** (2020) 006, [[arXiv:1912.09982](#)].
- [40] S. Alioli, A. Broggio, A. Gavardi, S. Kallweit, M. A. Lim, R. Nagar, D. Napoletano, and L. Rottoli, *Resummed predictions for hadronic Higgs boson decays*, *JHEP* **04** (2021) 254, [[arXiv:2009.13533](#)].
- [41] R. Mondini, M. Schiavi, and C. Williams,  *$N^3LO$  predictions for the decay of the Higgs boson to bottom quarks*, *JHEP* **06** (2019) 079, [[arXiv:1904.08960](#)].
- [42] G. Dissertori, A. Gehrmann-De Ridder, T. Gehrmann, E. W. N. Glover, G. Heinrich, and H. Stenzel, *Precise determination of the strong coupling constant at NNLO in QCD from the three-jet rate in electron-positron annihilation at LEP*, *Phys. Rev. Lett.* **104** (2010) 072002, [[arXiv:0910.4283](#)].
- [43] G. Dissertori, A. Gehrmann-De Ridder, T. Gehrmann, E. W. N. Glover, G. Heinrich, G. Luisoni, and H. Stenzel, *Determination of the strong coupling constant using matched NNLO+NLLA predictions for hadronic event shapes in  $e^+e^-$  annihilations*, *JHEP* **08** (2009) 036, [[arXiv:0906.3436](#)].
- [44] A. Gehrmann-De Ridder, T. Gehrmann, E. W. N. Glover, and G. Heinrich, *NNLO corrections to event shapes in  $e^+e^-$  annihilation*, *JHEP* **12** (2007) 094, [[arXiv:0711.4711](#)].
- [45] A. Gehrmann-De Ridder, T. Gehrmann, E. W. N. Glover, and G. Heinrich, *NNLO moments of event shapes in  $e^+e^-$  annihilation*, *JHEP* **05** (2009) 106, [[arXiv:0903.4658](#)].
- [46] J. Gao, *Probing light-quark Yukawa couplings via hadronic event shapes at lepton colliders*, *JHEP* **01** (2018) 038, [[arXiv:1608.01746](#)].
- [47] J. Gao, Y. Gong, W.-L. Ju, and L. L. Yang, *Thrust distribution in Higgs decays at the next-to-leading order and beyond*, *JHEP* **03** (2019) 030, [[arXiv:1901.02253](#)].
- [48] M.-X. Luo, V. Shtabovenko, T.-Z. Yang, and H. X. Zhu, *Analytic Next-To-Leading Order Calculation of Energy-Energy Correlation in Gluon-Initiated Higgs Decays*, *JHEP* **06** (2019) 037, [[arXiv:1903.07277](#)].
- [49] J. Gao, V. Shtabovenko, and T.-Z. Yang, *Energy-energy correlation in hadronic Higgs decays: analytic results and phenomenology at NLO*, *JHEP* **02** (2021) 210, [[arXiv:2012.14188](#)].
- [50] A. Djouadi, J. Kalinowski, and P. M. Zerwas, *Higgs radiation off top quarks in high-energy  $e^+e^-$  colliders*, *Z. Phys. C* **54** (1992) 255–262.

- [51] K. G. Chetyrkin, B. A. Kniehl, and M. Steinhauser, *Decoupling relations to  $O(\alpha_s^3)$  and their connection to low-energy theorems*, *Nucl. Phys. B* **510** (1998) 61–87, [[hep-ph/9708255](#)].
- [52] K. G. Chetyrkin, J. H. Kuhn, and C. Sturm, *QCD decoupling at four loops*, *Nucl. Phys. B* **744** (2006) 121–135, [[hep-ph/0512060](#)].
- [53] Y. Schroder and M. Steinhauser, *Four-loop decoupling relations for the strong coupling*, *JHEP* **01** (2006) 051, [[hep-ph/0512058](#)].
- [54] P. A. Baikov, K. G. Chetyrkin, and J. H. Kühn, *Five-Loop Running of the QCD coupling constant*, *Phys. Rev. Lett.* **118** (2017), no. 8 082002, [[arXiv:1606.08659](#)].
- [55] J. A. M. Vermaseren, S. A. Larin, and T. van Ritbergen, *The four loop quark mass anomalous dimension and the invariant quark mass*, *Phys. Lett. B* **405** (1997) 327–333, [[hep-ph/9703284](#)].
- [56] A. Gehrmann-De Ridder, T. Gehrmann, E. W. N. Glover, and G. Heinrich, *EERAD3: Event shapes and jet rates in electron-positron annihilation at order  $\alpha_s^3$* , *Comput. Phys. Commun.* **185** (2014) 3331, [[arXiv:1402.4140](#)].
- [57] A. Gehrmann-De Ridder, T. Gehrmann, E. W. N. Glover, and G. Heinrich, *Jet rates in electron-positron annihilation at  $O(\alpha_s^3)$  in QCD*, *Phys. Rev. Lett.* **100** (2008) 172001, [[arXiv:0802.0813](#)].
- [58] J. M. Campbell, M. A. Cullen, and E. W. N. Glover, *Four jet event shapes in electron-positron annihilation*, *Eur. Phys. J. C* **9** (1999) 245–265, [[hep-ph/9809429](#)].
- [59] A. Gehrmann-De Ridder, T. Gehrmann, and E. W. N. Glover, *Antenna subtraction at NNLO*, *JHEP* **09** (2005) 056, [[hep-ph/0505111](#)].
- [60] A. Gehrmann-De Ridder, T. Gehrmann, E. W. N. Glover, and G. Heinrich, *Infrared structure of  $e^+e^- \rightarrow 3\text{jets}$  at NNLO*, *JHEP* **11** (2007) 058, [[arXiv:0710.0346](#)].
- [61] J. Kuipers, T. Ueda, J. A. M. Vermaseren, and J. Vollinga, *FORM version 4.0*, *Comput. Phys. Commun.* **184** (2013) 1453–1467, [[arXiv:1203.6543](#)].
- [62] C. Anastasiou, F. Herzog, and A. Lazopoulos, *The fully differential decay rate of a Higgs boson to bottom-quarks at NNLO in QCD*, *JHEP* **03** (2012) 035, [[arXiv:1110.2368](#)].
- [63] V. Del Duca, C. Duhr, G. Somogyi, F. Tramontano, and Z. Trócsányi, *Higgs boson decay into b-quarks at NNLO accuracy*, *JHEP* **04** (2015) 036, [[arXiv:1501.07226](#)].
- [64] A. Gehrmann-De Ridder, T. Gehrmann, and E. W. N. Glover, *Gluon-gluon antenna functions from Higgs boson decay*, *Phys. Lett. B* **612** (2005) 49–60, [[hep-ph/0502110](#)].

- [65] R. Boughezal, J. M. Campbell, R. K. Ellis, C. Focke, W. Giele, X. Liu, F. Petriello, and C. Williams, *Color singlet production at NNLO in MCFM*, *Eur. Phys. J. C* **77** (2017), no. 17, [[arXiv:1605.08011](#)].
- [66] J. Campbell and T. Neumann, *Precision Phenomenology with MCFM*, *JHEP* **12** (2019) 034, [[arXiv:1909.09117](#)].
- [67] C. R. Schmidt,  *$H \rightarrow ggg(gq\bar{q})$  at Two Loops in the Large- $M_t$  Limit*, *Phys. Lett. B* **413** (1997) 391–395, [[hep-ph/9707448](#)].
- [68] X. Chen, J. Cruz-Martinez, T. Gehrmann, E. W. N. Glover, and M. Jaquier, *NNLO QCD corrections to Higgs boson production at large transverse momentum*, *JHEP* **10** (2016) 066, [[arXiv:1607.08817](#)].
- [69] G. Coloretti, *Event shapes in hadronic higgs decays*, Master’s thesis, ETH Zürich, 2021.
- [70] J. Alwall, M. Herquet, F. Maltoni, O. Mattelaer, and T. Stelzer, *MadGraph 5: Going Beyond*, *JHEP* **06** (2011) 128, [[arXiv:1106.0522](#)].
- [71] J. Alwall, R. Frederix, S. Frixione, V. Hirschi, F. Maltoni, O. Mattelaer, H. S. Shao, T. Stelzer, P. Torrielli, and M. Zaro, *The automated computation of tree-level and next-to-leading order differential cross sections, and their matching to parton shower simulations*, *JHEP* **07** (2014) 079, [[arXiv:1405.0301](#)].
- [72] F. Buccioni, J.-N. Lang, J. M. Lindert, P. Maierhöfer, S. Pozzorini, H. Zhang, and M. F. Zoller, *OpenLoops 2*, *Eur. Phys. J. C* **79** (2019), no. 10 866, [[arXiv:1907.13071](#)].
- [73] J. Pires and E. W. N. Glover, *Double real radiation corrections to gluon scattering at NNLO*, *Nucl. Phys. B Proc. Suppl.* **205-206** (2010) 176–181, [[arXiv:1006.1849](#)].
- [74] E. W. Nigel Glover and J. Pires, *Antenna subtraction for gluon scattering at NNLO*, *JHEP* **06** (2010) 096, [[arXiv:1003.2824](#)].
- [75] **ALEPH** Collaboration, D. Buskulic et al., *Studies of QCD in  $e^+e^- \rightarrow$  hadrons at  $E_{\text{cm}} = 130$  and 136 GeV*, *Z. Phys. C* **73** (1997) 409–420.
- [76] **ALEPH** Collaboration, A. Heister et al., *Studies of QCD at  $e^+e^-$  centre-of-mass energies between 91 GeV and 209 GeV*, *Eur. Phys. J. C* **35** (2004) 457–486.
- [77] D. Wicke, J. Drees, and K. Hamacher, *Energy Dependence of Event Shapes and of  $\alpha_s$  at LEP 2*, .
- [78] **DELPHI** Collaboration, J. Abdallah et al., *A Study of the energy evolution of event shape distributions and their means with the DELPHI detector at LEP*, *Eur. Phys. J. C* **29** (2003) 285–312, [[hep-ex/0307048](#)].

- [79] **DELPHI** Collaboration, J. Abdallah et al., *The Measurement of  $\alpha_s$  from event shapes with the DELPHI detector at the highest LEP energies*, *Eur. Phys. J. C* **37** (2004) 1–23, [[hep-ex/0406011](#)].
- [80] **L3** Collaboration, M. Acciarri et al., *Study of the structure of hadronic events and determination of  $\alpha_s$  at  $\sqrt{s} = 130$  GeV and 136 GeV*, *Phys. Lett. B* **371** (1996) 137–148.
- [81] **L3** Collaboration, M. Acciarri et al., *QCD studies and determination of  $\alpha_s$  in  $e^+e^-$  collisions at  $\sqrt{s} = 161$  GeV and 172 GeV*, *Phys. Lett. B* **404** (1997) 390–402.
- [82] **L3** Collaboration, M. Acciarri et al., *QCD results from studies of hadronic events produced in  $e^+e^-$  annihilations at  $\sqrt{s} = 183$  GeV*, *Phys. Lett. B* **444** (1998) 569–582.
- [83] **L3** Collaboration, P. Achard et al., *Determination of  $\alpha_s$  from hadronic event shapes in  $e^+e^-$  annihilation at  $192 \text{ GeV} \leq \sqrt{s} \leq 208 \text{ GeV}$* , *Phys. Lett. B* **536** (2002) 217–228, [[hep-ex/0206052](#)].
- [84] **L3** Collaboration, P. Achard et al., *Studies of hadronic event structure in  $e^+e^-$  annihilation from 30 GeV to 209 GeV with the L3 detector*, *Phys. Rept.* **399** (2004) 71–174, [[hep-ex/0406049](#)].
- [85] **OPAL** Collaboration, P. D. Acton et al., *A Determination of  $\alpha_s(M_{Z_0})$  at LEP using Resummed QCD Calculations*, *Z. Phys. C* **59** (1993) 1–20.
- [86] **OPAL** Collaboration, G. Alexander et al., *QCD studies with  $e^+e^-$  annihilation data at 130 GeV and 136 GeV*, *Z. Phys. C* **72** (1996) 191–206.
- [87] **OPAL** Collaboration, K. Ackerstaff et al., *QCD studies with  $e^+e^-$  annihilation data at 161 GeV*, *Z. Phys. C* **75** (1997) 193–207.
- [88] **OPAL** Collaboration, G. Abbiendi et al., *QCD studies with  $e^+e^-$  annihilation data at 172 GeV – 189 GeV*, *Eur. Phys. J. C* **16** (2000) 185–210, [[hep-ex/0002012](#)].
- [89] **OPAL** Collaboration, G. Abbiendi et al., *Measurement of event shape distributions and moments in  $e^+e^- \rightarrow$  hadrons at 91 GeV – 209 GeV and a determination of  $\alpha_s$* , *Eur. Phys. J. C* **40** (2005) 287–316, [[hep-ex/0503051](#)].
- [90] S. Catani, L. Trentadue, G. Turnock, and B. R. Webber, *Resummation of large logarithms in  $e^+e^-$  event shape distributions*, *Nucl. Phys. B* **407** (1993) 3–42.
- [91] P. F. Monni, T. Gehrmann, and G. Luisoni, *Two-Loop Soft Corrections and Resummation of the Thrust Distribution in the Dijet Region*, *JHEP* **08** (2011) 010, [[arXiv:1105.4560](#)].
- [92] A. Banfi, H. McAslan, P. F. Monni, and G. Zanderighi, *A general method for the resummation of event-shape distributions in  $e^+e^-$  annihilation*, *JHEP* **05** (2015) 102, [[arXiv:1412.2126](#)].

- [93] A. Banfi, H. McAslan, P. F. Monni, and G. Zanderighi, *The two-jet rate in  $e^+e^-$  at next-to-next-to-leading-logarithmic order*, *Phys. Rev. Lett.* **117** (2016), no. 17 172001, [[arXiv:1607.03111](#)].
- [94] N. Baberuxki, C. T. Preuss, D. Reichelt, and S. Schumann, *Resummed predictions for jet-resolution scales in multijet production in  $e^+e^-$  annihilation*, *JHEP* **04** (2020) 112, [[arXiv:1912.09396](#)].
- [95] J. Baglio and A. Djouadi, *Higgs production at the LHC*, *JHEP* **03** (2011) 055, [[arXiv:1012.0530](#)].
- [96] C. Anastasiou, K. Melnikov, and F. Petriello, *Fully differential Higgs boson production and the di-photon signal through next-to-next-to-leading order*, *Nucl. Phys. B* **724** (2005) 197–246, [[hep-ph/0501130](#)].
- [97] S. Brandt, C. Peyrou, R. Sosnowski, and A. Wroblewski, *The Principal axis of jets. An Attempt to analyze high-energy collisions as two-body processes*, *Phys. Lett.* **12** (1964) 57–61.
- [98] E. Farhi, *A QCD Test for Jets*, *Phys. Rev. Lett.* **39** (1977) 1587–1588.
- [99] G. Parisi, *Super Inclusive Cross-Sections*, *Phys. Lett. B* **74** (1978) 65–67.
- [100] J. F. Donoghue, F. E. Low, and S.-Y. Pi, *Tensor Analysis of Hadronic Jets in Quantum Chromodynamics*, *Phys. Rev. D* **20** (1979) 2759.
- [101] S. Catani and B. R. Webber, *Resummed  $C$  parameter distribution in  $e^+e^-$  annihilation*, *Phys. Lett. B* **427** (1998) 377–384, [[hep-ph/9801350](#)].
- [102] P. E. L. Rakow and B. R. Webber, *Transverse Momentum Moments of Hadron Distributions in QCD Jets*, *Nucl. Phys. B* **191** (1981) 63–74.
- [103] S. Catani, G. Turnock, and B. R. Webber, *Jet broadening measures in  $e^+e^-$  annihilation*, *Phys. Lett. B* **295** (1992) 269–276.
- [104] L. Clavelli and D. Wyler, *Kinematical Bounds on Jet Variables and the Heavy Jet Mass Distribution*, *Phys. Lett. B* **103** (1981) 383–387.
- [105] S. Catani, Y. L. Dokshitzer, M. Olsson, G. Turnock, and B. R. Webber, *New clustering algorithm for multi-jet cross-sections in  $e^+e^-$  annihilation*, *Phys. Lett. B* **269** (1991) 432–438.
- [106] N. Brown and W. J. Stirling, *Jet cross-sections at leading double logarithm in  $e^+e^-$  annihilation*, *Phys. Lett. B* **252** (1990) 657–662.
- [107] N. Brown and W. J. Stirling, *Finding jets and summing soft gluons: A New algorithm*, *Z. Phys. C* **53** (1992) 629–636.

- [108] W. J. Stirling, *Hard QCD working group: Theory summary*, *J. Phys. G* **17** (1991) 1567–1574.
- [109] S. Bethke, Z. Kunszt, D. E. Soper, and W. J. Stirling, *New jet cluster algorithms: Next-to-leading order QCD and hadronization corrections*, *Nucl. Phys. B* **370** (1992) 310–334. [Erratum: *Nucl.Phys.B* 523, 681–681 (1998)].
- [110] S. Frixione and B. R. Webber, *Matching NLO QCD computations and parton shower simulations*, *JHEP* **06** (2002) 029, [[hep-ph/0204244](#)].
- [111] P. Nason, *A New method for combining NLO QCD with shower Monte Carlo algorithms*, *JHEP* **11** (2004) 040, [[hep-ph/0409146](#)].